NOSOLOGIC IMAGING OF BRAIN TUMORS USING MRI AND MRSI

Jan Luts, Teresa Laudadio, Albert J. Idema, Arjan W. Simonetti, Arend Heerschap, Dirk Vandermeulen, Johan A.K. Suykens, and Sabine Van Huffel

ABSTRACT

INTRODUCTION

EXPERIMENTAL

- Data
- A two-step segmentation-classification framework
- MRI segmentation
  - Generating a subject-specific abnormal tissue prior from MRSI and MRI
  - Segmentation based on the modified atlas
- Classification of the abnormal region
  - Determination of the type of abnormal tissue
  - Pattern recognition methods

RESULTS

- Analysis of the patient data
- Subject-specific abnormal tissue prior

DISCUSSION

CONCLUSIONS

ACKNOWLEDGEMENTS

REFERENCES

TABLES

CAPTIONS OF FIGURES

ABSTRACT

A new technique is presented to create nosologic images of the brain based on magnetic resonance imaging and magnetic resonance spectroscopic imaging (MRSI). A nosologic image summarizes the presence of different tissues and lesions in a single image by color coding each voxel or pixel according to the histopathological class it is assigned to. The proposed technique applies advanced methods from image processing as well as pattern recognition to segment and classify brain tumors. First, a registered brain atlas and a subject-specific abnormal tissue prior, obtained from MRSI data, are used for the segmentation. Next, the detected abnormal tissue is classified based on supervised pattern recognition methods. Class probabilities are also calculated for the segmented abnormal region. Compared to previous approaches, the new framework is more flexible and able to better exploit spatial information leading to improved nosologic images. The combined scheme offers a new way to produce high-resolution nosologic images, representing tumor heterogeneity and class probabilities, which may help clinicians in decision making.

INTRODUCTION

Contrast-enhanced magnetic resonance imaging (MRI) is an important tool for the anatomical assessment of brain tumors. As a consequence, automatic brain tumor segmentation based on MRI is a widely studied topic (Kaus *et al.*, 2001; Warfield *et al.*, 1998). Nowadays, techniques based on thresholds, region growing, clustering, Markov random fields, classification algorithms, and artificial neural networks have been used and accurate segmentation results have been reported after comparison with manual tumor segmentation by an expert. However, several diagnostic questions, such as the type and grade of the tumor, are difficult to address using conventional MRI. The histopathological characterization of a tissue specimen remains the gold standard, despite the associated risks of surgery to obtain a biopsy. In recent years, the use of magnetic resonance spectroscopy (MRS), which provides metabolic information, is increasingly being used for more detailed and specific noninvasive evaluation of brain tumors. In particular magnetic resonance spectroscopic imaging (MRSI), which provides quantitative metabolite maps of the brain, is attractive as this may also enable to visualize the heterogeneous spatial extent of tumors, both inside and outside the MRI detectable lesion.

However, the individual inspection and analysis of the many spectral patterns, obtained by MRSI, remains extremely time-consuming and requires specific spectroscopic expertise. Therefore, it is not practical in a clinical setting, where automated processing and evaluation of the MRSI data as well as easy and rapid display of the results as images or maps are needed for routine clinical interpretation of an exam.

As such, the term nosologic image was introduced for an image which indicates a specific tissue type in a certain color (Szabo de Edelenyi *et al.*, 2000). Szabo de Edelenyi *et al.* (2000) used pattern recognition techniques and combined one specific contrast from MRI with spectroscopic information. Simonetti *et al.* (2003) combined additional image variables with the metabolic information to construct nosologic images. Both studies used the combination of MRI and MRSI for new, more relevant brain tumor classifiers, but treated each pixel or voxel of the nosologic image independently, only exploiting the spectral information and image intensities. Therefore, Laudadio *et al.* (2008) proposed the application of canonical correlation analysis (CCA) to MRSI data as a way to include spatial information when producing nosologic images. Afterwards, Kelm (2007) suggested to apply conditional random fields to MRSI data since the technique by Laudadio *et al.* (2008) uses a sliding window which can cancel out effects from isolated voxels and some long-range interactions are lacking because of the fixed window size. Kelm (2007) claimed that his approach, based on a global method, is able to increase the performance of single voxel classifiers by at least 15%.

In this study, we extend previous work to construct improved, high-resolution nosologic images. The new scheme benefits from both advanced image processing methods, producing an improved segmented image, and sophisticated classification methods from pattern recognition. The framework comprises a segmentation step and a classification step where MRSI and MRI data are simultaneously exploited, thereby yielding improved

segmentation and classification results. Furthermore, spatial information is included in both steps and class probabilities are also generated.

EXPERIMENTAL

Data

Data coming from 24 patients with a brain tumor and 4 healthy volunteers were selected from the INTERPRET project database. The MRI and MRSI data were acquired in the University Medical Center Nijmegen (UMCN). The study was approved by the ethical committee of the UMCN and followed the rules of theWorld Health Organization (WHO). All data passed a strict quality control and the tumor type was determined by histopathological consensus. To create a sufficiently large training data set for the pattern recognition methods, several voxels, situated in the tumor area, were selected from each patient based on histological, radiological, and spectroscopic information (Devos *et al.*, 2005). Voxels for a specific tissue class were only selected from patients for which this tissue type was confirmed by a histopathological consensus, performed by three independent pathologists. Because of the heterogeneity of brain tumors, the MRI data and the spectral information were taken into account during the selection of voxels. For this purpose, for each patient all the high-resolution MR images were plotted together with the MRSI spectra and a segmented image in which voxels from MRSI were clustered by a model-based algorithm using a graphical user interface. Since the clustering provided an objective segmentation, this was considered to be helpful for voxel selection. Based on all these data sources, an expert in MR spectroscopy selected voxels if they were clearly within the affected brain region, avoiding contamination from normal cerebral tissue,

such that spectra under consideration were found to be typical for that pathology. Normal brain MR spectra typically have a large NAA peak around 2 ppm and almost equal peaks around 3.2 and 3.03 ppm, respectively, choline and creatine. Cerebrospinal fluid (CSF) would show no signal in the spectra, but due to partial volume effects, profiles, similar to normal MR spectra, are often visible but with lower intensities. On the other hand, tumor MR spectra have elevated choline compared with creatine. Grade II gliomas have a large myo-inositol peak at 3.57 ppm, and elevated choline compared with creatine. Grade III glioma MR spectra have an intermediary pattern between grade II glioma and glioblastoma MR spectra. Glioblastoma MR spectra reveal dominant lipid/lactate peaks around 0.9 and 1.3 ppm. Some high-grade tumors have higher choline, and in general there is a large range of lipid and metabolite concentrations. Meningiomas are characterized by a number of almost equally sized peaks, broad peaks centered around 2.3 and 3.78 ppm, which most likely comprise glutamate, glutamine and macromolecules, choline (3.2 ppm), and various amounts of signal at 0.9 and 1.3 ppm, macromolecules/lipid/lactate. Following standard radiological MRI features, tumor is normally hypointense on a T1-weighted image and hyperintense on a T2- and proton density-weighted image, while contrast enhancement usually indicates higher grade tissue for gliomas. CSF is hypointense on a T1-weighted image, hyperintense on a T2-weighted image, and isointense on a proton density-weighted image. Necrosis is usually hypointense and shows no contrast enhancement. Although this method was subjective, it was chosen because tumors are known to be heterogeneous and because there is no "ground truth" in the diagnosis of brain tumors at the voxel level. Also, spectra from CSF and normal tissue measured from volunteers and patients were selected. Six classes of

pathology were considered: normal brain tissue from volunteers and apparently normal tissue from the contralateral half of the brain of patients (218 voxels from 8 persons), CSF (100 voxels from 8 patients), grade II glioma (176 voxels from 10 patients), grade III glioma (69 voxels from 5 patients), grade IV glioma (70 voxels from 7 patients), and meningioma (48 voxels from 3 patients).

The data were acquired on a 1.5 T Siemens Vision Scanner with CP-head coil. Four MR images were acquired, namely T1-weighted image (TE/TR = 15/644 ms), T2-weighted image (TE/TR = 98/3100 ms), proton density-weighted image (TE/TR = 16/3100 ms) and gadolinium enhanced T1-weighted image (15 ml 0.5M Gd-DTPA), with matrix size equal to 256 × 256. Both water-suppressed and unsuppressed proton MR spectroscopic images were measured using a 2D STEAM sequence with the STEAM box positioned totally in the brain (16 × 16 × 1024 samples, TR/TE/TM = 2000 or 2500/20/30 ms, slice thickness = 12.5 or 15 mm, FOV = 200 mm, spectral width = 1000 Hz and NS = 2). Disturbing signals arising from the fat tissue surrounding the skull were avoided. The location of the STEAM box was determined using the gadolinium enhanced T1-weighted image showing the largest tumor area. The MRSI slice was centered around an MRI slice of 5 mm.

MR image registration was performed based on the algorithm described in Maes *et al.* (1997). It was assumed that the MRSI data were registered with the proton density-weighted image since they were acquired in a consecutive manner. Preprocessing of MRSI included filtering of k-space data by a Hanning filter of 50 % using the LUISE

software package (Siemens, Erlangen, Germany), zero filling to 32 × 32, spatial 2D Fourier transformation to obtain time domain signals for each voxel, correction for eddy current effects by a technique which prevents occasional occurrence of eddy current correction induced artifacts (Simonetti *et al.*, 2002), frequency alignment, water removal using HLSVD from 4.3 ppm to 5.5 ppm (Pijnappel *et al.*, 1992), and a simple baseline correction using an exponential filter with a width of 5 ms followed by subtraction of the residual of the original signal. All first order phases were corrected by first manually optimizing the mean spectrum which was calculated from all spectra in the STEAM box of each patient's MRSI data. Next, this correction was applied to each separate signal of the patient's MRSI data. Finally, the spectra were normalized using the water signal. For each metabolite signal, a corresponding water-unsuppressed signal was available, acquired with the same acquisition parameters as the metabolite signal and originating from the same voxel. The amplitude of the water-unsuppressed signal was estimated by a nonlinear least squares algorithm (Devos *et al.*, 2004). The water-unsuppressed signal was modeled in the time domain by a Voigt model, with an additional first order term that corrected for eddy currents. HSVD was used to obtain initial parameter estimates, which were subsequently used as starting values in a nonlinear least squares algorithm to obtain the final parameter estimates. Each spectral value in the preprocessed water-suppressed spectrum was divided by the obtained estimate of the intensity of the water peak.

In this study, an input pattern for pattern recognition was a set of features extracted from the spectrum in combination with MRI pixel intensities. First, the magnitude spectrum

was computed and the spectral points within the frequency range (0.5–4 ppm) were considered. Figure 1 depicts the water-normalized mean magnitude spectra, along with the standard deviation, for each of the tissue types in the data set. Next, ten different features were extracted, using peak integration within a spectral range, from each spectrum (Govindaraju *et al.*, 2000): lipids (0.835–0.965 ppm), lipids (1.2 ppm) and lactate + alanine (1.265–1.395 ppm), N-acetylaspartate (1.955–2.085 ppm), glutamate + glutamine (2.135–2.265 ppm), creatine (2.955–3.095 ppm), choline (3.135–3.265 ppm), taurine + glucose (3.375–3.505 ppm), myo-inositol + glycine (3.495–3.625 ppm), glutamate + glutamine + alanine (3.685–3.815 ppm), and creatine (3.885–4.015 ppm). These ten values, referred to as the peak-integrated values in the rest of this chapter, were combined with four MRI variables obtained by lowering the resolution of the four MR images to the one of the MRSI grid by averaging pixel intensities within each voxel as in Simonetti *et al.* (2003).

A two-step segmentation-classification framework

In this chapter, we propose a two-step segmentation-classification framework able to simultaneously exploit MRI and MRSI data. In particular, the first step was performed based on the segmentation method presented by Prastawa *et al.* (2004). The required input for that method was a T2-weighted image. No contrast-enhanced images were needed, but additional types of MR images could be used to improve the segmentation. More precisely, Prastawa *et al.* (2004) proposed a method consisting of three stages: abnormality detection using a digital brain atlas and outlier detection; edema detection based on the T2-weighted image intensities; application of geometric and spatial

constraints to the detected edema and tumor regions. In our new framework, we included additional information from MRSI to improve the abnormal tissue detection for segmentation. Specifically, as described in the next section, in addition to the standard brain atlas, a subject-specific abnormal tissue prior was generated by applying a supervised pattern recognition technique to the available MRSI (and MRI) data set. In the second step of the segmentation-classification framework all pixels from the detected abnormal region were classified based on supervised pattern recognition techniques and nosologic images were provided as final result, where each tissue type was denoted by a specific color. The two-step framework is explained in the following paragraphs.

MRI segmentation

Generating a subject-specific abnormal tissue prior from MRSI and MRI

In a digital brain atlas, only probabilities are provided for the healthy tissue classes: white matter, gray matter, and CSF. The study in Prastawa *et al.* (2003) proposed the inclusion of a subject-specific abnormal tissue prior by means of the contrast-enhanced image. In this study, we generated a subject-specific prior for the abnormal tissue as well, but based on a linear discriminant analysis (LDA) classifier. Indeed, in Luts *et al.* (2007) it was shown that a simple linear classifier was sufficient to separate abnormal tissue from healthy tissue. Therefore, we applied LDA (trained on all available training data except data coming from the case under study) to the grid of feature vectors containing 14 entries, that is ten bicubically interpolated peak-integrated values (such that it matched with the size of the MRI grid) and the four types of MRI pixel intensities. For each pixel within the area of the STEAM box, LDA predicted whether there was abnormal or

healthy tissue based on all peak-integrated values and the MRI pixel intensities. The lower left panel of Figure 2 depicts the resulting grid that was generated by the LDA classifier for case 4. For illustration purposes, the choline over creatine ratio, obtained by the interpolated peak-integrated values, is depicted in the right panel of the middle row.

Next, the output from LDA was integrated into the original digital brain atlas by setting the abnormal prior, if abnormal tissue was predicted by the LDA method, to a probability derived from that classifier. If no abnormal tissue was predicted by LDA, the abnormal prior was set to a fraction of the white matter and gray matter atlas probabilities as in Prastawa *et al.* (2004). Since the MRSI information was restricted to the STEAM box, the abnormal tissue prior was only available within that area. Every prior probability outside that box was obtained as in Prastawa *et al.* (2004). In the results section, it is demonstrated that the addition of the abnormal tissue prior improves the segmentation procedure.

Segmentation based on the modified atlas

After the prior was generated, part of the segmentation approach from Prastawa *et al.* (2004) was followed. Abnormal tissue was detected using an iterative procedure. First a threshold was used on the posterior probabilities, or atlas probabilities in the first iteration, and pixels in high confidence regions were sampled. Next, the samples from normal tissue that exceeded a distance threshold, based on the minimum covariance determinant (MCD) estimator, were removed. A nonparametric model was used to estimate the probability density functions from the samples. The posterior probabilities

were calculated based on the subject-specific atlas priors and the estimated densities. To conclude an iteration of abnormality detection, a bias field correction was performed because of the presence of the image inhomogeneity. The bias field was estimated from the white and gray matter probabilities and the full procedure was repeated. After the separation of abnormality, an edema detection stage was proposed in the framework in Prastawa *et al.* (2004). The detection was done using the T2-weighted image, assuming that edema has high fluid content and appears brighter than the tumor. We decided to remove this stage from our segmentation step since, after validation of the results, it seemed that cysts, which were also brighter on the T2 image, were often segmented as edema. Also, it is known that edema in glioma tumors is often infiltrated and therefore this tissue should be detected as abnormal. The last stage of the segmentation step was reclassification with spatial and geometric constraints. For this purpose region competition snakes were used (Ho *et al.*, 2002). First, a threshold was used on the posterior probabilities and a sampling was performed. The tumor samples were pruned based on the level-set evolution after which the densities were estimated. New posterior class probabilities were calculated; the bias field was corrected and the procedure was repeated.

Classification of the abnormal region

Determination of the type of abnormal tissue

After segmentation, white matter, gray matter, CSF, and abnormal tissue were separated. To provide additional information about the tumor type that was present within the abnormal tissue region, a supervised pattern recognition step was introduced. As for the

subject-specific abnormal tissue prior, the MRSI data (e.g. spectra, peak-integrated values) were interpolated to match the size of the MRI data. Naturally, only pixels within the STEAM box could be classified. More precisely, all pixels, found to be abnormal by the segmentation step, were classified into one of the tumor categories that were represented in the training set for pattern recognition. This means that for this specific study, we were able to detect white matter, gray matter, CSF, and, based on spectroscopic profiles, grade II glioma, grade III glioma, grade IV glioma, and meningioma.

Pattern recognition methods

Concerning classification, basically every (semi-)supervised pattern recognition method can be incorporated, which makes the framework very flexible. Here, we decided to focus on kernel logistic regression (KLR) (Karsmakers *et al.*, 2007), a multiclass classifier using Bayesian least squares support vector machines (LS-SVMs) (Luts *et al.*, 2007) and CCA. Bayesian LS-SVMs (Van Gestel *et al.*, 2002) and KLR were used since these kernel-based methods were able to provide class probabilities instead of "black or white" decisions. CCA was included because it was able to exploit spatial information (Laudadio *et al.*, 2008). The methods are briefly discussed in the following paragraph.

Standard LS-SVMs (Suykens and Vandewalle, 1999) can only handle binary classification problems and produce binary output scores. In Luts *et al.* (2007) it was proposed to combine binary Bayesian LS-SVMs with radial basis function (RBF) kernel into a multiclass classifier system. Based on binary classifiers and pairwise combination algorithms multiclass probabilities were retrieved. Following the findings in Luts *et al.*

(2007), the combination method of Wu *et al.* (2004) was used to combine pairwise class probabilities. Direct multiclass probabilities were generated using KLR. In Karsmakers *et al.* (2007) it was shown that the optimization problem for KLR could be solved by a weighted version of LS-SVMs. From the practical point of view this means that KLR does not need to construct binary classifiers; one direct multiclass solution can be obtained. Finally, CCA was included since the method exploits spatial information, that is based on the information in the neighboring pixels, a decision is made for the center pixel. Since CCA was applied to the interpolated grid (within the abnormal tissue region), we reduced the risk to average out the effect of isolated tumor voxels by the information that was present in the neighborhood as compared to (Laudadio *et al.*, 2008). The symmetric 3×3 model without corner voxels was used as spatial model and PCA was applied as subspace model.

RESULTS

A leave-one-person-out validation analysis was performed to evaluate the framework. For the creation of the abnormal tissue prior and for the classification step, all data from the test subject were removed from the training set. As such, model selection was performed on all data except for the voxels coming from the subject under study. In the next paragraph, nosologic images are reported and the use of class probabilities is illustrated. Finally, the use of the abnormal tissue prior is explained. Table 1 provides an overview of the patients' data.

Analysis of the patient data

The framework was applied to generate nosologic images for nine patients (Figures 2 and 3). Light blue reflects white matter, dark blue gray matter, green CSF, yellow grade II glioma, orange grade III glioma, dark red glioblastoma, and purple meningioma. All classification results in this section were generated using feature vectors where peak-integrated values were combined with image intensities. To demonstrate the flexibility of the framework, and more specifically the flexibility of the classification step, the use of various pattern recognition methods is illustrated. Nevertheless, it is worth stressing that the goal of the present study is not to compare the different pattern recognition methods, but to show that any type of classifier can be integrated in the classification step, or can be used for generating the additional subject-specific abnormal tissue prior in the segmentation step. The flexibility property shown here is very important as, based on the specific problem under investigation, ad hoc classification methods could be applied.

Cases 6–8 represent patients with a glioblastoma multiforma tumor as assigned by the pathologists. The nosologic images, obtained by applying a Bayesian LS-SVM classifier, show that the method was able to detect the tumor lesions and glioblastoma tissue (Figure 3). These examples also show that edema and/or tumor infiltration is difficult to assess. In diffuse astrocytoma, the peritumoral edema is presumed infiltrated by glioma tumor cells. In these cases, the differentiation between pure infiltration and pure edema cannot be made. As discussed before the segmentation of edema was not consistent and was left out of the procedure and so no edema is shown in the nosologic images. In heterogeneous tumors, like gliomas, this distinction cannot be made with conventional MRI techniques. Therefore, the most likely assignment for this abnormal tissue is low grade glioma. Low

grade tumor next to glioblastoma is pathologically possible. In case 8, there are two tumor areas. The posterior part could include a hematoma, identified by an arrow, within the tumor. For the surrounding tissue it is difficult to distinguish edema from infiltrating tumor.

Cases 3, 4, and 5 are good examples of the difficult differentiation between WHO grade II and grade III glioma brain tumor. The histopathological diagnosis for case 3 was grade II glioma. The framework, applying CCA in the classification step, found the correct tissue type, despite the enhancement after contrast for small parts of the tumor at the occipital parts of the insula (Figure 3). For case 4, the pathologists disagreed between a grade II and a grade III glial tumor. The nosologic image, created using a Bayesian LS-SVM classifier, shows a heterogeneous tumor with mainly grade III glioma, according to the spectroscopic classifier, especially in the part with enhancement after gadolinium (Figure 2). The differentiation between grade II glioma and edema at the frontal and medial parts cannot be made. The use of class probabilities is illustrated by means of a contour plot. Blue contour lines show higher grade III glioma probabilities as opposed to red contour lines. The grade III glioma probabilities are higher at the frontal part of the abnormal tissue region with the enhancement after gadolinium and smaller at the occipital part of the tumor in case 4. For case 5 with an anaplastic oligodendroglioma, CCA was used (Figure 3). Almost only low grade glioma, WHO grade II was found with a small region of anaplastic glioma, WHO grade III. This would be an underestimation of the real situation. At surgery, a debulking of the tumor was performed. Therefore, the

pathological diagnosis was not from only the small part with a nosological anaplastic tumor.

Case 2 is a diffuse low grade astrocytoma, grade II, with no enhancement after contrast and good segmentation of the tumor/tumor infiltration/edema based on KLR (Figure 3). For case 1 the histopathological agreement was grade II glioma, despite the enhancement after gadolinium. The Bayesian LS-SVM method was used and it detected the correct tissue type (Figure 3). However, in this case no edema and/or tumor infiltration was detected which was very reliable around the enhancing spot. The nosologic image for case 9 with a meningioma tumor was obtained by the CCA classifier (Figure 3). In this case, the small edema part at the occipital part of the tumor was not classified as abnormal tissue. In the case of a low grade meningioma there is no infiltration.

Subject-specific abnormal tissue prior

During the detection of abnormality step a sampling for gray matter, white matter, and CSF was done based on the atlas priors. The bottom row (second panel from the left) of Figure 2 depicts the selected samples for the healthy tissue classes (i.e. gray matter, white matter, and CSF) following the modified digital brain atlas for case 4. It can be observed that, in contrast to the approach in Prastawa *et al.* (2004), almost no samples for healthy tissue were picked from the tumor area after the subject-specific abnormal tissue prior was added to the standard atlas. The extra prior clearly improves the sampling and, as a consequence, reduces the contamination reported in Prastawa *et al.* (2004). As a result, improved sampling leads to higher quality prototypes for all the tissue classes and better

density estimates in the detection of the abnormality step. Finally, an example (case 3) of the difference between the two approaches with respect to the final segmentation is provided (Figure 4). In contrast to the panels on the right, no abnormal tissue prior was added to the digital brain atlas to produce the left images. The top row summarizes the information that was available in the atlas before starting segmentation. This result was generated by choosing the tissue type with the highest prior probability based on the (modified) atlas. The lower row shows the final result after segmentation. CSF is colored green, white matter light blue, gray matter dark blue, and abnormal tissue is red. Before starting segmentation, one can observe that there was only a region for which the probabilities of abnormal tissue were higher than the ones of the normal classes in the digital brain atlas that was modified with the subject-specific abnormal tissue prior. After segmentation, and when comparing with the MRI of case 3 (Figure 2) only a small part of the abnormal tissue region was detected by the original segmentation algorithm that just included healthy tissue priors. By introducing the extra prior from MRSI, the abnormal tissue region was better recognized. The MR spectra confirmed the existence of abnormal tissue in that area.

DISCUSSION

In MRI-based segmentation of tissue in the brain, a digital brain atlas is an important, additional, tool to resolve the problem of overlap between intensity distributions of different tissue types. Since a digital brain atlas only contains priors for the healthy tissue classes, researchers attempted to include a prior for the abnormal tissue as well. Typically, the contrast-enhanced T1-weighted image is used for this purpose (Prastawa *et*

al., 2003). However, it is known that blood vessels also generally appear enhanced. In addition, tumors may show only partially signal enhancement and some tumors do not enhance at all. For this reason, we decided to use the MRSI data to generate the prior for tissue abnormality. Although the spatial resolution of MRSI is low compared to MRI, it appeared that MRSI was very useful for defining the prior and that it could improve the original segmentation algorithm described in Prastawa *et al.* (2004). Indeed, in Prastawa *et al.* (2004) it was explained that the segmentation algorithm could only deal with a limited amount of brain deformation. During the detection of abnormality step sampling is initially based on the atlas. The outliers are detected based on the MCD method and the density functions are estimated. However, when there is a serious brain deformation, the brain atlas leads to incorrect sampling since pixels for the healthy tissue classes are sampled from the abnormal tissue regions. In this case, the samples are severely contaminated and the MCD algorithm may not yield correct results, leading to incorrect estimated densities. Figures 2 and 4 illustrate this and show that the use of the abnormal tissue prior, generated from MRSI, is advantageous.

In general, the proposed framework highlights the advantages of a method able to exploit and combine different types of information. In particular, our study shows the value of adding MRSI over MRI data, of adding MRI over MRSI information, and the improvements achieved in the segmentation and classification approaches with respect to their previously proposed versions. For instance, several diagnostic questions, such as the type and grade of the tumor, are difficult to address using MRI, but MRSI data permit taking the corresponding metabolic differences into account. Therefore, using MRSI

information over just MRI has the additional advantage that nosologic images (specifying the type of the tumor) can be obtained, instead of the results (which only localize the tumor) obtained with classical MRI segmentation approaches.

The added value of MRI over just MRSI has already been evaluated in a number of studies, which concluded that combining MRI with MRSI features improved the performance of the classifiers (Devos *et al.*, 2005; Galanaud *et al.*, 2006; Simonetti *et al.*, 2005). For this reason, in the present study, the four MR images were also used in the classification step. Furthermore, adding MRI over MRSI data, allowed to perform the segmentation step based on high-resolution MRI data. We found that this improved the detection of CSF compared to pure segmentation of MRSI data and also that gray matter and white matter were detected based on MRI. In contrast, the CCA approach by Laudadio *et al.* (2008) only performed a segmentation on the MRSI data. CCA is an interesting method since it is able to simultaneously exploit the spectral-spatial information provided by the MRSI data and is computationally efficient. On the other hand, the disadvantage of this approach is that the same spatial constraints (i.e. a fixed spatial model) are used for every voxel of the MRSI grid, without taking into account whether the voxel is on the border or the middle of the tumor. In simulation studies, we found that this can lead to wrong classifications for rather isolated tumor voxels. In the proposed framework, CCA was applied after the segmentation step, that is after the tumor was detected, reducing the risk of misclassification for rather isolated tumor voxels. Therefore, the above issue is improved by making use of image processing methods that incorporate more advanced spatial constraints, based on the high-resolution MRI data.

The use of these spatial constraints in the current method is also an improvement compared to the approaches where every pixel or voxel was classified separately, ignoring this prior knowledge (Luts *et al.*, 2007; Simonetti *et al.*, 2003; Szabo de Edelenyi *et al.*, 2000).

On the other hand, as proven by biopsies, outside the abnormal tissue on the conventional MRI image, infiltrating tumor cells can be found with and without abnormal spectroscopic findings (Croteau *et al.*, 2001; Ganslandt *et al.*, 2005; Li *et al.*, 2002; Price *et al.*, 2007). Therefore, the whole infiltrating tumor is not always taken into account. Price *et al.* (2007) showed a biopsy-guided improved delineation of glioma tumors with diffusion tensor imaging. Also, the segmentation of edema in glioma tumors is not straightforward. To distinguish edema from tumor the intensity of a T2-weighted image is not sufficient. This does not always differentiate tumor cysts, resection cysts, or cerebral fluid from pure edema. Next to this, in glioma tumors the peritumoral edema is mostly infiltrated by tumor cells and the intensity differences between edema and tumor are on a sliding scale. With the available information in this study no specific segmentation of peritumoral edema and tumor could be made for glioma tumors. Therefore, this segmentation step was not used. Ricci *et al.* (2007) showed metabolic changes in peritumoral edema with MR spectroscopy. The combination of diffusion tensor imaging and MR spectroscopy might be helpful to improve the delineation of glioma tumors and differentiation of edema and infiltrating tumor.

The differentiation between WHO grade II and grade III is radiologically very difficult. According to the WHO-2007 classification (Louis *et al.*, 2007), the main histopathological difference between WHO grade II and III diffuse astrocytic neoplasms is increased mitotic activity in the latter. Therefore, it is not surprising that one third of the non-enhancing diffuse gliomas are histopathologically diagnosed as high-grade lesions at the time of biopsy (Barker *et al.*, 2000). The value of the addition of MR spectroscopy for the differentiation of WHO grade II and grade III gliomas is currently not clear (McKnight *et al.*, 2007; Stadlbauer *et al.*, 2006). However, in part this could be due to the underestimation of the brain tumor malignancy in tumors diagnosed by biopsies (Jackson *et al.*, 2001). By including perfusion and diffusion MR data the differentiation may be improved (Di Costanzo *et al.*, 2006; Law *et al.*, 2003).

Although precise estimation of peak integrals is difficult due to peak overlap and noise, features were extracted from the spectra based on simple peak integration. Therefore, spectral fitting methods might seem more appropriate. However, prior to the application of the two-step framework, the classification accuracies of different spectral fitting methods and peak integration were compared. Since the quantification approaches did not improve classifier performance and since these methods were more time-consuming, we decided to use peak integration. Some previous studies also reported no increase in classifier performance for quantification methods compared to automated approaches as for instance principal component analysis (Kelm, 2007; Simonetti *et al.*, 2005). A related issue is determining the number of features to extract from the spectra. In this study, we extracted a common set of features which are in general known to be relevant for the

classification problems under study. Although the focus of the present work was the development of the methodology of the framework, this is an issue that can be improved and it is still open for discussion. As such, future work could focus on the optimization of these data preprocessing steps as this can potentially further increase the performance of the total framework that is presented here.

In this study, only one of the MRI slices was totally included within the MRSI slice. For this reason, the framework only combined one MRI slice with the MRSI data. However, in practice, depending on its size, multiple MRI slices may be needed to cover the whole tumor. As such, a potential improvement of the existing framework could be the extension to three-dimensional MRSI data with the inclusion of multiple MRI slices. Also, in the present study the standard image orientation protocol in the radiology service was used in order to limit the acquisition time. If a different orientation is used, a better enclosure of the brain tumor mass may be obtained, such that the framework that is presented here provides further improved nosologic images.

CONCLUSIONS

This study proposes a new method to generate nosologic images of the brain by exploiting and combining MRI and MRSI data. Advanced methods from image processing and pattern recognition are combined in a two-step approach. In the first step, segmentation is performed by means of a modified version of the method described in Prastawa *et al.* (2004), by including a subject-specific abnormal tissue prior, derived from MRI and MRSI, in the original brain atlas. The subject-specific abnormal tissue prior is

found to improve the segmentation procedure. The segmentation step provides an image of the slice of interest where white matter, gray matter, CSF, and the abnormal region are clearly visualized. Next, the abnormal tissue is classified using pattern recognition and class probabilities are generated for the diverse tissue types. The method is applied to various patients with different types of brain tumors. Compared to previous approaches that generate nosologic images, the use of spatial information and prior knowledge is further improved in the proposed method. The framework offers a new way to visualize tumor heterogeneity and class probabilities in a single nosologic image, assisting clinicians in decision making.

ACKNOWLEDGEMENTS

NMR in Biomedicine and John Wiley and Sons are gratefully acknowledged for the license agreement. This research is funded by a PhD grant of the Institute for the Promotion of Innovation through Science and Technology in Flanders (IWT-Vlaanderen); Research supported by Research Council KUL: GOA-MaNet, GOA-AMBioRICS, several PhD/postdoc & fellow grants, Centers-of-excellence optimisation, IDO 05/010 EEG-fMRI, GOA/2004/05 (Mixing and Analyzing Real and Virtual Environments and Lighting); Institute for Molecules and Materials, Analytical Chemistry, Chemometrics Research Department of the Radboud University Nijmegen for preprocessing the MRSI data; Flemish Government: FWO: PhD/postdoc grants, projects, G.0360.05 (Advanced EEG analysis techniques for epilepsy monitoring), G.0519.06 (Noninvasive brain oxygenation), G.0341.07 (Data fusion), G.0321.06 (Numerical tensor techniques for spectral analysis), G.0302.07 (Support vector machines and kernel methods), G.0566.06 (Computational strategies for shape modeling and matching and

their application in medical image analysis), research communities (ICCoS, ANMMM); IWT: PhD Grants; Belgian Federal Government: DWTC (IUAP IV-02 (1996-2001), IUAP V-22 (2002-2006): Dynamical Systems and Control: Computation, Identification & Modelling) and Belgian Federal Science Policy Office IUAP P6/04 (Dynamical systems, control and optimization, 2007-2011); EU: INTERPRET project (contract no. IST-1999-10310) is gratefully acknowledged, Marinette van der Graaf and Maarten Aerts are gratefully acknowledged, BIOPATTERN (contract no. FP6-2002-IST 508803), eTUMOUR (contract no. FP6-2002-LIFESCIHEALTH 503094), HealthAgents (contract no. FP6-2005-IST 027213), FAST (contract no. FP6-019279-2), ESA: Cardiovascular Control (Prodex-8 C90242).

REFERENCES

Barker, F.G. II, Chang, S.M., Huhn, S.L., Davis, R.L., Gutin, P.H., McDermott, M.W., Wilson, C.B., and Prados, M.D. 2000. Age and the risk of anaplasia in magnetic resonance-nonenhancing supratentorial cerebral tumors. Cancer 80: 936-941.

Croteau, D., Scarpace, L., Hearshen, D., Gutierrez, J., Fisher, J.L., Rock, J.P., and Mikkelsen, T. 2001. Correlation between magnetic resonance spectroscopy imaging and image-guided biopsies: Semiquantitative and qualitative histopathological analyses of patients with untreated glioma. Neurosurgery 49: 823-829.

Devos, A., Lukas, L., Suykens, J.A.K., Vanhamme, L., Tate, A.R., Howe, F.A., Majos, C., Moreno-Torres, A., van der Graaf, M., Arus, C., and Van Huffel, S. 2004. Classification of brain tumours using short echo time 1H MR spectra. J. Magn. Reson. 170: 164-175.

Devos, A., Simonetti, A.W., van der Graaf, M., Lukas, L., Suykens, J.A.K., Vanhamme, L., Buydens, L.M.C., Heerschap, A., and Van Huffel, S. 2005. The use of multivariate MR imaging intensities versus metabolic data from MR spectroscopic imaging for brain tumour classification. J. Magn. Reson. 173: 218-228.

Di Costanzo, A., Scarabino, T., Trojsi, F., Giannatempo, G.M., Popolizio, T., Catapano, D., Bonavita, S., Maggialetti, N., Tosetti, M., Salvolini, U., d'Angelo, V.A., and Tedeschi, G. 2006. Multiparametric 3T MR approach to the assessment of cerebral gliomas: tumor extent and malignancy. Neuroradiology 48: 622-631.

Galanaud, D., Nicoli, F., Chinot, O., Confort-Gouny, S., Figarella-Branger, D., Roche, P., Fuentes, S., Le Fur, Y., Ranjeva, J.-P., and Cozzone, P.J. 2006. Noninvasive diagnostic assessment of brain tumors using combined in vivo MR imaging and spectroscopy. Magn. Reson. Med. 55: 1236-1245.

Ganslandt, O., Stadlbauer, A., Fahlbusch, R., Kamada, K., Buslei, R., Blumcke, I., Moser, E., and Nimsky, C. 2005. Proton magnetic resonance spectroscopic imaging integrated into image-guided surgery: correlation to standard magnetic resonance imaging and tumor cell density. Neurosurgery 56: 291-298.

Govindaraju, V., Young, K., and Maudsley, A.A. 2000. Proton NMR chemical shifts and coupling constants for brain metabolites. NMR Biomed. 13: 129-153.

Ho, S., Bullitt, E., and Gerig, G. 2002. Level-set evolution with region competition: Automatic 3-D segmentation of brain tumors. In Proceedings of the 16th International Conference on Pattern Recognition. Quebec, 532-535.

Jackson, R.J., Fuller, G.N., Abi-Said, D., Lang, F.F., Gokaslan, Z.L., Shi, W.M., Wildrick, D.M., and Sawaya, R. 2001. Limitations of stereotactic biopsy in the initial management of gliomas. Neuro Oncol. 3: 193–200.

Karsmakers, P., Pelckmans, K., and Suykens, J.A.K. 2007. Multi-class kernel logistic regression: a fixed-size implementation. In Proceedings of the 20th International Joint Conference on Neural Networks. Orlando, 1756-1761.

Kaus, M., Warfield, S.K., Nabavi, A., Black, P.M., Jolesz, F.A., and Kikinis, R. 2001. Automated segmentation of MRI of brain tumors. Radiology 218: 586-591.

Kelm, B.M. 2007. Evaluation of vector-valued clinical image data using probabilistic graphical models: quantification and pattern recognition. Ph.D. Thesis, University of Heidelberg.

Laudadio, T., Martinez-Bisbal, M.C., Celda, B., and Van Huffel, S. 2008. Fast nosological imaging using canonical correlation analysis of brain data obtained by two-dimensional turbo spectroscopic imaging. NMR Biomed. 21: 311-321.

Law, M., Yang, S., Wang, H., Babb, J.S., Johnson, G., Cha, S., Knopp, E.A., and Zagzag, D. 2003. Glioma grading: Sensitivity, specificity, and predictive values of perfusion MR imaging and proton MR spectroscopic imaging compared with conventional MR imaging. Am. J Neuroradiol. 24: 1989-1998.

Li, X., Lu, Y., Pirzkall, A., McKnight, T.R., and Nelson, S.J. 2002. Analysis of the spatial characteristics of metabolic abnormalities in newly diagnosed glioma patients. J. Magn. Reson. Imaging 16: 229-237.

Louis, D.N., Ohgaki, H., Wiestler, O.D., and Cavenee, W.K. 2007. World Health Organization Classification of Tumours of the Central Nervous System. IARC: Lyon.

Luts, J., Heerschap, A., Suykens, J.A.K., and Van Huffel, S. 2007. A combined MRI and MRSI based multiclass system for brain tumour recognition using LS-SVMs with class probabilities and feature selection. Artif. Intell. Med. 40: 87-102.

Maes, F., Collignon, A., Vandermeulen, D., Marchal, G., and Suetens, P. 1997. Multimodality image registration by maximization of mutual information. IEEE Trans. Med. Imaging 16: 187-198.

McKnight, T.R., Lamborn, K.R., Love, T.D., Berger, M.S., Chang, S., Dillon, W.P., Bollen, A., and Nelson, S.J. 2007. Correlation of magnetic resonance spectroscopic and growth characteristics within grades II and III gliomas. J Neurosurg. 106: 660-666.

Pijnappel, W.W.F., van den Boogaart, A., de Beer, R., and van Ormondt, D. 1992. SVD-based quantification of magnetic resonance signals. J. Magn. Reson. 97: 122-134.

Prastawa, M., Bullitt, E., Moon, N., Van Leemput, K., and Gerig, G. 2003. Automatic brain tumor segmentation by subject specific modification of atlas priors. Acad. Radiol. 10: 1341-1348.

Prastawa, M., Bullitt, E., Ho, S., and Gerig, G. 2004. A brain tumor segmentation framework based on outlier detection. Med. Image Anal. 8: 275-283.

Price, S.J., Jena, R., Burnet, N.G., Hutchinson, P.J., Dean, A.F., Pena, A., Pickard, J.D., Carpenter, T.A., and Gillard, J.H. 2006. Improved delineation of glioma margins

and regions of infiltration with the use of diffusion tensor imaging: an image-guided biopsy study. Am. J. Neuroradiol. 27: 1969-1974.

Ricci, R., Bacci, A., Tugnoli, V., Battaglia, S., Maffei, M., Agati, R., and Leonardi, M. 2007. Metabolic findings on 3T 1H-MR spectroscopy in peritumoral brain edema. Am. J. Neuroradiol. 28: 1287-1291.

Simonetti, A.W., Melssen, W.J., van der Graaf, M., Heerschap, A., and Buydens, L.M.C. 2002. Automated correction of unwanted phase jumps in reference signals which corrupt MRSI spectra after eddy current correction. J. Magn. Reson. 159: 151-157.

Simonetti, A.W., Melssen, W.J., van der Graaf, M., Heerschap, A., and Buydens, L.M.C. 2003. A new chemometric approach for brain tumor classification using magnetic resonance imaging and spectroscopy. Anal. Chem. 75: 5352-5361.

Simonetti, A.W., Melssen, W.J., Szabo de Edelenyi, F., van Asten, J.J.A., Heerschap, A., and Buydens, L.M.C. 2005. Combination of feature-reduced MR spectroscopic and MR imaging data for improved brain tumor classification. NMR Biomed. 18: 34-43.

Stadlbauer, A., Gruber, S., Nimsky, C., Fahlbusch, R., Hammen, T., Buslei, R., Tomandl, B., Moser, E., and Ganslandt, O. 2006. Preoperative grading of gliomas by using metabolite quantification with high-spatial-resolution proton MR spectroscopic imaging. Radiology 238: 958-969.

Suykens, J.A.K., and Vandewalle, J. 1999. Least squares support vector machine classifiers. Neural Process. Lett. 9(3): 293-300.

Szabo de Edelenyi, F., Rubin, C., Esteve, F., Grand, S., Decorps, M., Lefournier, V., Le Bas, J.F., and Remy, C. 2000. A new approach for analyzing proton magnetic resonance spectroscopic images of brain tumors: nosologic images. Nat. Med. 6: 1287-1289.

Van Gestel, T., Suykens, J.A.K., Lanckriet, G., Lambrechts, A., De Moor, B., and Vandewalle, J. 2002. Bayesian framework for least squares support vector machine classifiers, Gaussian processes and kernel Fisher discriminant analysis. Neural Comput. 14: 1115-1147.

Warfield, S.K., Kaus, M., Jolesz, F.A., and Kikinis, R. 2000. Adaptive template moderated spatially varying statistical classification. Med. Image Anal. 4: 43-55.

Wu, T., Lin, C., and Weng, R. 2004. Probability estimates for multi-class classification by pairwise coupling. J. Mach. Learn. Res. 5: 975-1005.

TABLES

Table 1: Pathology, tumor grade, age, and sex for 9 subjects.

Case	Pathology	Grade	Age	Sex
1	Diffuse astrocytoma	II	58	Female
2	Diffuse astrocytoma	II	39	Male
3	Oligoastrocytoma	II	42	Male
4	Oligodendroglioma	II/III	41	Female
5	Oligodendroglioma	III	30	Female
6	Glioblastoma	IV	53	Male
7	Glioblastoma	IV	54	Male
8	Glioblastoma	IV	50	Male
9	Meningioma	I	45	Female

CAPTIONS OF FIGURES

Figure 1: Mean water-normalized magnitude MR spectra for normal tissue, CSF, grade II gliomas, grade III gliomas, meningiomas, and glioblastomas. The solid lines are the means, while the dotted lines are the means plus the standard deviations.

Figure 2: Case 4, grade II/III glioma. Top row: T1-weighted MR image, T2-weighted MR image, proton density-weighted MR image, and gadolinium enhanced T1-weighted MR image. The arrow identifies the enhanced area. Middle row: T2-weighted MR image and MR spectra originating from the identified area, choline over creatine ratio map (high ratios are white). Bottom row: probabilities for abnormal tissue generated by the LDA classifier (high probabilities are white) to create subject-specific abnormal tissue prior, selected samples for healthy tissue classes, nosologic image (light blue = white matter, dark blue = gray matter, green = CSF, yellow = grade II glioma, orange = grade III glioma), contour plot for grade III glioma (blue = high probability, red = low probability). Grade III glioma probabilities are higher at the frontal part of the abnormal tissue region with the enhancement after gadolinium and smaller at the occipital part of the tumor.

Figure 3: MR image and nosologic image for case 1, 2, 3, 5, 6, 7, 8, and 9. Light blue reflects white matter, dark blue gray matter, green CSF, yellow grade II glioma, orange grade III glioma, dark red glioblastoma, and purple meningioma. The hematoma for case 8 is identified by an arrow.

Figure 4: The effect of using a subject-specific abnormal tissue prior based on MRSI for case 3. The results on the left are generated without an abnormal tissue prior in contrast to the results on the right. The top row shows the prior probabilities from the atlas, the bottom row the final segmentation result. The abnormal tissue is only correctly recognized by the segmentation algorithm that includes the extra abnormal tissue prior from MRSI.

Figure 1

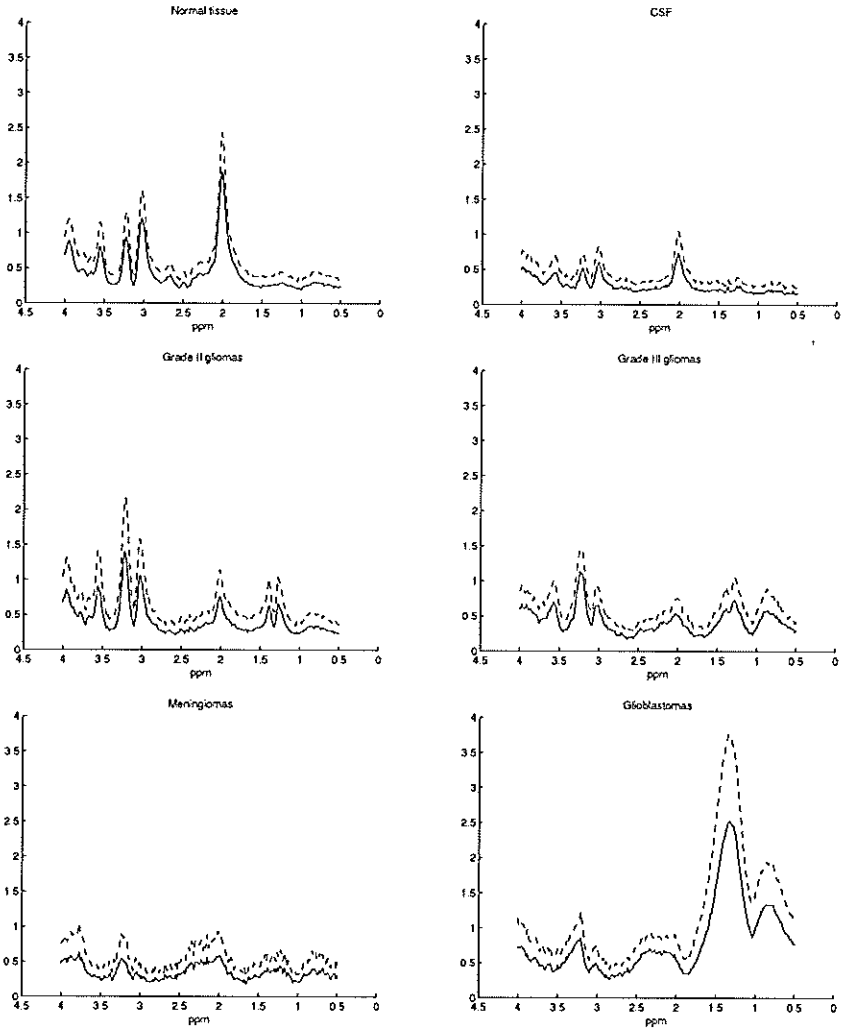

Normal tissue
CSF
Grade II gliomas
Grade III gliomas
Meningiomas
Glioblastomas
ppm

Figure 2

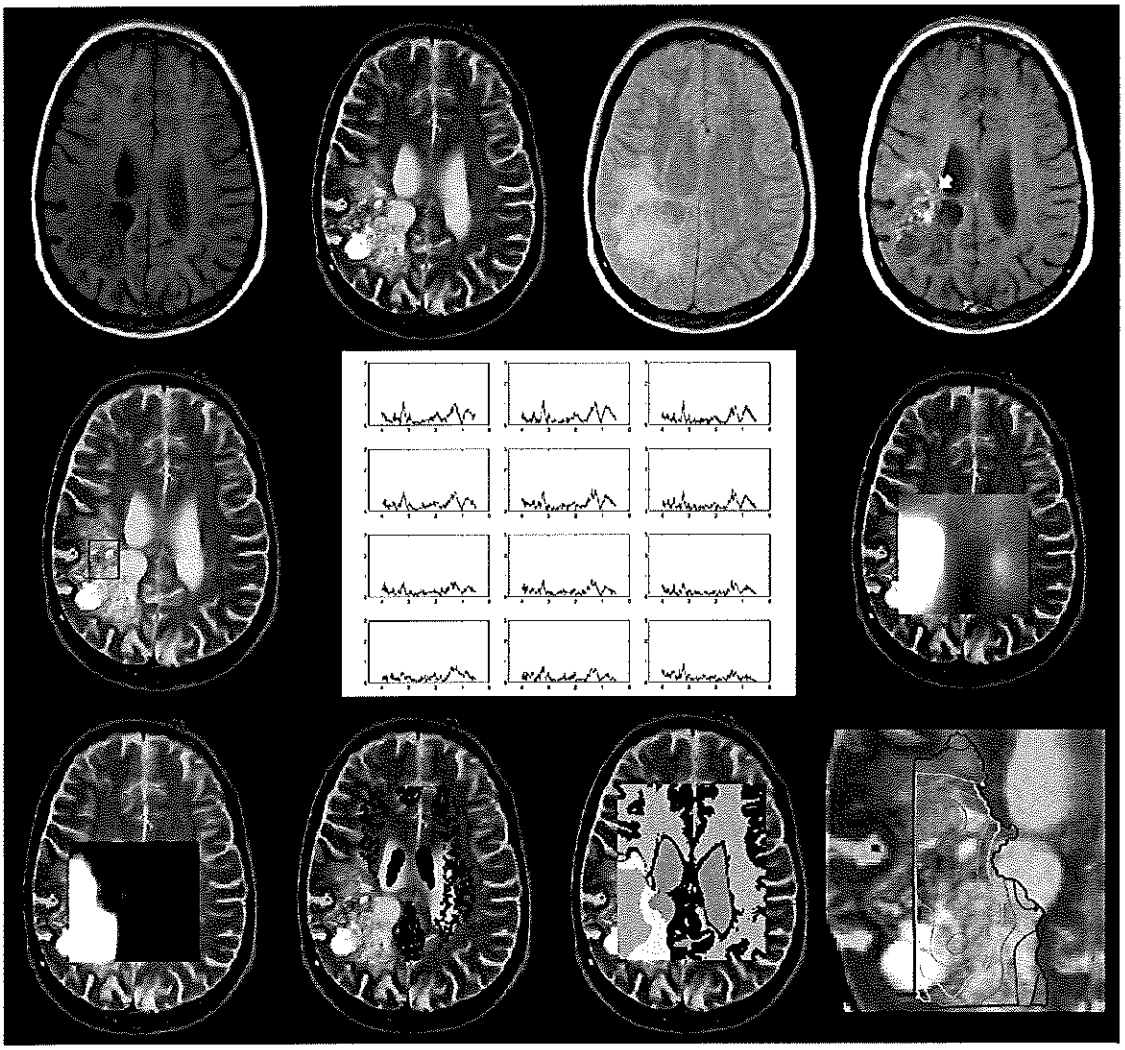


Figure 3

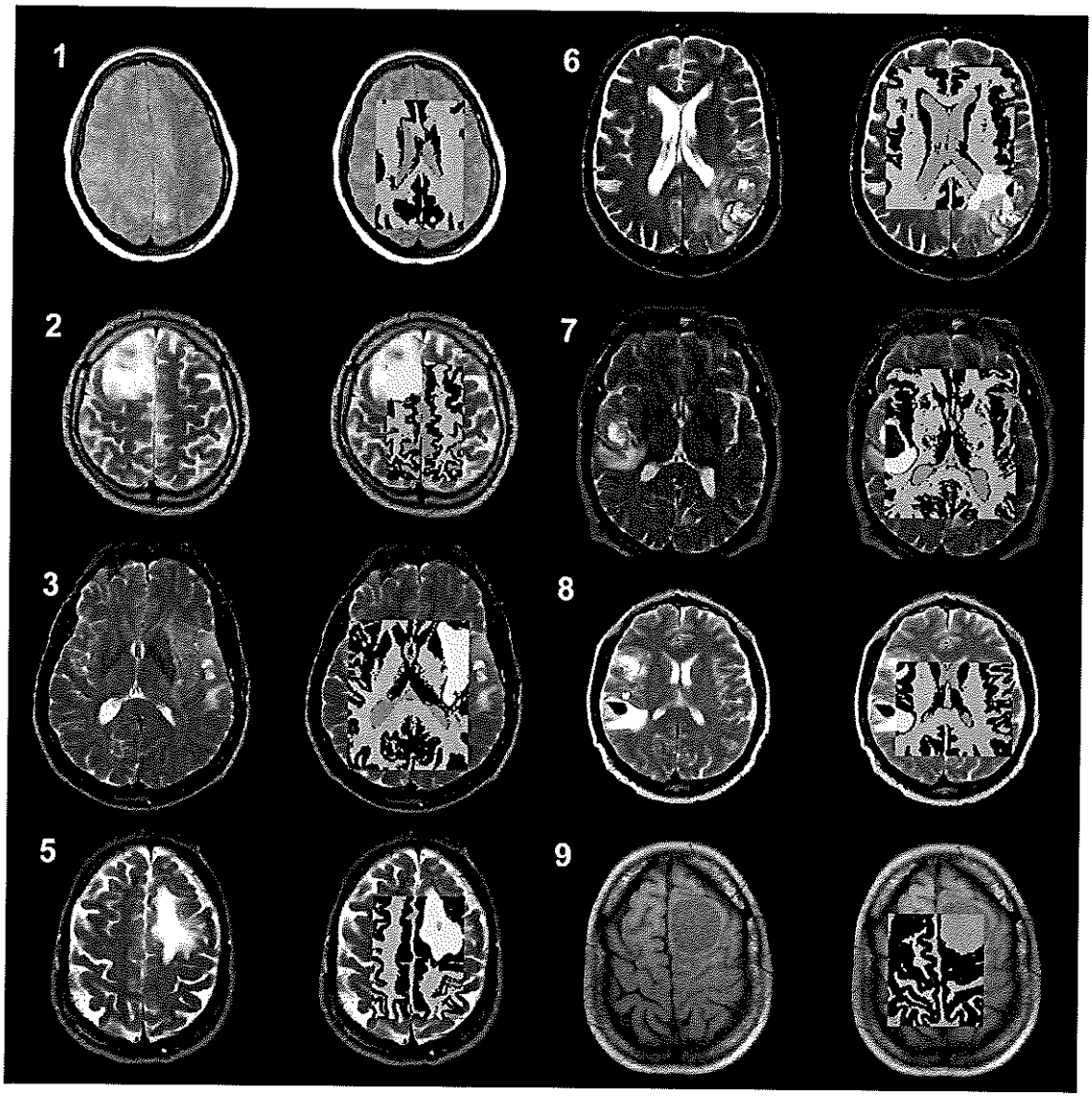


Figure 4

